Transpiration Velocities Based Sheet Cavitation Model

Surasak Phoemsapthawee, Jean-Baptiste Leroux, Jean-Marc Laurens
Laboratoire Brestois des Mécaniques et des Systèmes (LBMS) - EA4325, ENSIETA[1]

François Deniset
Institut de Recherche de l'Ecole Navale (IRENav) - EA3634, Ecole Navale

Abstract

A partial sheet cavitation model is developed and implemented within a 3D BEM code in order to estimate the hydrodynamics forces and performance of a propeller or a rudder working in an unsteady flow environment. The model proposes a relationship between the sheet cavitation geometry and the pressure distribution in subcavitating conditions. The model is validated in the first stage by comparing its results with 2D measured pressure coefficient distributions and 3D measured cavity length distributions available in the literature. In the last stage of validation in steady-state flow conditions, experimental trials consisting in measuring the lift and drag coefficients of a 3D hydrofoil are performed. The measured lift and drag coefficients as well as the comparison with the numerical results are reported. In unsteady-state flow conditions, applications of propellers and rudders were simulated to demonstrate the performance of the model.

Keywords

Sheet cavitation, Propellers, Hydrofoils, Unsteady, Hydrostatic pressure, Hydrodynamic force

1 Introduction

Sheet cavitation is known to affect the hydrodynamic performances of propellers. It also produces severe pressure fluctuation. Since many ships operate and will increasingly operate in heavily loaded conditions, there is a real need for cavitating propeller simulations in the unsteady-state operating mode. It coincides with the arising of complex viscous two-phase flow simulation capability. The VIRTUE program (Salvatore et al., 2009a) involves several of these viscous two-phase flow simulations around a propeller. Although some convincing results are obtained, the required computing resources are still considered substantial. Furthermore, the use of a viscous two-phase flow solver still requires a cavitation model with some degrees of assumption and simplification. The full understanding of cavitation and its simulation would require a model at the molecular scale.

In order to model sheet cavitation, some understanding of this phenomenon is required. One important point of the phenomenon is how the cavity develops on lifting bodies with a round leading edge. Unlike downstream sharp-corner bodies, the mechanism is arguable. Franc (1986), argues based on experimental observations that the leading-edge sheet cavitation requires a laminar-boundary-layer separation and that the cavity develops downstream of the laminar-boundary-layer separation point. This mechanism is widely accepted and used as the cavity detachment criterion for many sheet cavitation simulations, see for instance: Briançon-Marjolet and Merle (1999), Salvatore and Esposito (2001), Brewer and Kinnas (1997).

Nevertheless, Farhat et al. (2002) demonstrate that sheet cavitation can occur with another mechanism. According to the experimental results obtained at the "Laboratoire de Machines Hy-

[1]ENSIETA, 2 rue François Verny 29806 Brest Cedex9 France, laurenje@ensieta.fr

drauliques, Ecole Polytechnique Fédérale de Lausanne", the sheet cavitation phenomenon has been observed without any sign of laminar-boundary-layer separation. This observation might support the Brillouin-Villat criterion or in other words the smooth detachment criterion. This criterion, which consists in choosing the point which guarantees the curvature continuity while respecting the slippery condition and the steam pressure condition, is used by most simulations, for example: Kinnas and Fine (1993), Lee and Kinnas (2004).

Once sheet cavitation has developed, some assumptions for pressure distribution must be made in order to compute the hydrodynamic forces. Most, if not all models, assume that, as in the boundary layer, the pressure does not vary between the blade surface and the outer bound of the cavity. In other words, the pressure in the cavity is assumed to be equal to the homogeneity of the vapor pressure. As long as the sheet cavitation is partial, the effects on hydrodynamic coefficients are expected to be moderate. Carlton (2007) mentions the early work of Balhan (1951) where it is shown in Figure 1 that the lift coefficients C_L and the drag coefficients C_D of Kármán-Trefftz profiles vary in function of the cavitation number σ_V. When the cavitation number σ_V decreases, the lift coefficient first increases slightly. And then it collapses when the cavitation number is such that the cavity does not close on the foil surface. It is generally admitted that the lift coefficient increases in presence of partial sheet cavitation and decreases abruptly when supercavitation occurs.

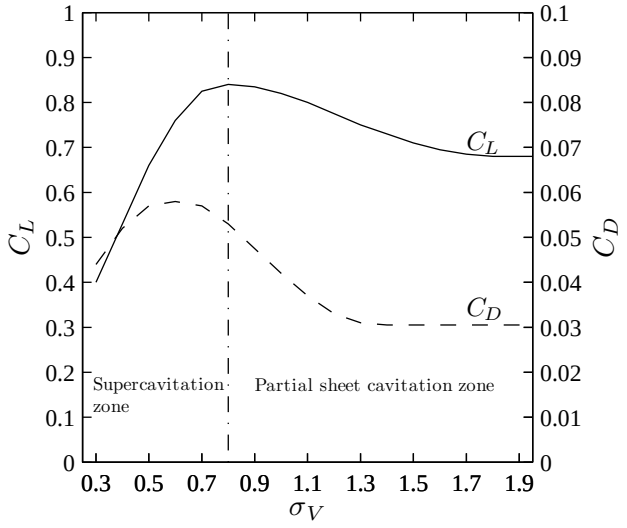

Figure 1: Effect of cavitation on the lift and drag coefficient of a Kármán-Trefftz profile; extracted from Balhan (1951)

This effect has been confirmed by many researchers. Several papers, some presented at the recent symposium on marine propulsors (SMP'09, Trondheim), report experimental results of the effect of sheet cavitation on propeller thrust and torque, see for instance: Jessup et al. (2009), Kanemaru and Ando (2009), as well as on hydrofoil lift and drag (Kato et al., 2006). All confirm the general trend obtained by Balhan (1951).

Another important point is the cavity closure mechanism. Experimental results, for example: Le et al. (1993) and Leroux (2003), show that the pressure distribution in the cavity closure region is not always constant and not necessarily equal to the vapor pressure. As the cavity can collapse into bubbles or cloud cavitation, some simulations use the Rayleigh's bubble collapse equation

as the cavity closure model (Yamaguchi and Kato, 1983). However, the cavity can also collapse with a re-entrant jet mechanism. Krishnaswamy et al. (2001) and Vaz et al. (2003) simulate this mechanism on 2D hydrofoils with the potential flow theory.

The cavity closure models used in potential flow simulations can be classified in two categories: open and closed models. Rowe and Blottiaux (1993) advanced the definition that a closed model is a model in which the streamline returns and touches the foil surface after having been deviated by the cavity, while an open model is a model in which the streamline does not retouch the foil surface after having been deviated by the cavity.

Although the partial sheet cavitation and the closed model are not necessarily identical, the closed model is most commonly used to simulate partial sheet cavitation, see for example Kinnas and Fine (1993); Briançon-Marjolet and Merle (1999); Salvatore and Esposito (2001); Peallat and Pellone (1996). Despite the difference of each model, the principle of the closed models is to transform the vapor pressure dynamic condition in a continuous manner on the cavity surface into a zero normal velocity condition on the wet surface.

In most sheet cavitation simulations in potential flow, see for instance Kinnas and Fine (1993); Salvatore and Esposito (2001); Vaz et al. (2003), the dipole strength distribution on the cavity planform is imposed by using the vapor pressure dynamic condition. The source strength distribution which represents the cavity thickness distribution is the unknown factor to be determined. Nevertheless, an iterative procedure is required to determine the cavity planform. To use such model, it assumes that one already has such a potential flow code at its disposal. As a consequence, the above model cannot be implemented in the direct potential flow codes in which the dipole strength distribution is the only unknown to be determined without any substantial rewriting of the code.

Since we are using this direct potential flow code, we have had to develop a specific sheet cavitation model compatible with our BEM code. Inspired by the method used in boundary layer simulation (Laurens, 1993), the cavitation model uses the transpiration velocities v^* which are perpendicular to the body panels to deviate the streamline in order to represent the presence of the cavity. The model is based on the existing relationship between the sheet cavitation geometry and the pressure distribution in subcavitating conditions. Unlike the simulations mentioned in the previous paragraph, the cavity planform is directly forced by the subcavitating pressure distribution. Yet, an iterative procedure is needed to determine the proper cavity thickness.

The present model takes the pressure fluctuation on the propeller blade into account but it is not intended to describe the physics of cavity. We are only interested in the effects of sheet cavitation on the hydrodynamic performance of the propellers. If one wants to access information concerning the acoustic of or/and damage to the propellers, the high frequency fluctuation of the cavity has to be modeled. This is the challenge of the next decade and some preliminary results have already been reported Salvatore et al. (2009b).

The developed cavitation model is then validated in two stages. The first stage of validation consists of comparing numerical results with experimental data and other numerical data available in literature. Nevertheless, for 3D flow cases, the available experimental data only allow qualitative comparisons of cavity lengths. As the objective of this development is to be able to estimate the effect of sheet cavitation on the hydrodynamic forces, a validation on hydrodynamic forces in 3D flow state is required. An experiment has been prepared and conducted in the cavitation tunnel of the Bulgarian Ship Hydrodynamic Centre (BSHC). The lift and drag coefficients of a partially cavitating 3D hydrofoil have been measured. The final stage of validation consists of the comparison between our numerical simulations and these experimental data.

Finally, simulations of cavitating hydrofoils and propellers in unsteady-state flow conditions

are also presented and discussed in order to study and demonstrate the performance of the cavitation model in unsteady-state flow conditions.

2 Presentation of cavitation model

As mentioned in the introduction, the sheet cavitation model has been developed for direct potential flow codes in which the source strength distribution is imposed directly by slippery condition and the dipole strength distribution is the unknown to be determined. The model uses the transpiration velocities technique in order to take into account the effect of partial sheet cavitation. These transpiration velocities v^* are equivalent to the additional source strengths which are simply added to the part of the surface carrying the cavity. Therefore, the implementation of the cavitation model in the potential flow codes is quite simple since it only requires the modification of the source strengths on the body surface where the cavity is, as shown in Equation 1. The problem is then the determination of this additional source strength distribution needed to properly simulate the cavity.

$$\sigma = \vec{U}_\infty \cdot \vec{n} + v^* \text{ on the cavity planform} \tag{1}$$

The core of the model is the function used to determine these transpiration velocities v^* distribution. We propose that a relationship exists between the cavity geometry and the pressure distribution in subcavitating conditions P_{sub}. Equation 2 describes the proposed relationship.

$$v^* = \frac{2k}{\rho U_\infty l} \int_{s_0}^{s} (P_V - P_{sub}) \, \mathrm{d}s \tag{2}$$

where k is an adaptive factor, U_∞ and l are the referent velocity and the referent length respectively, P_V is the vapor pressure, s is the curvilinear location and s_0 is the cavity detachment location.

The cavity thickness t_c or the cavity geometry is directly associated with the transpiration velocity v^* as shown in Equation 3.

$$t_c = \int_{s_0}^{s} \frac{v^*}{u_{sub}} \, \mathrm{d}s \quad ; \quad t_c \geq 0 \tag{3}$$

where u_{sub} is the tangential velocity in subcavitating conditions.

By using non-dimensional variables such as the pressure coefficient C_P and the cavitation number σ_V, Equation 2 can be rewritten in a more simple form as:

$$\tilde{v}^* = -k \int_{\tilde{s}_0}^{\tilde{s}} (C_P + \sigma_V) \, \mathrm{d}\tilde{s} \tag{4}$$

The general computation scheme is described as follows:

- Starting from the stagnation point and following the streamline, when the pressure in subcavitating conditions is greater than the vapor pressure ($P_{sub} > P_V$), the transpiration velocity is set to zero ($v^* = 0$) since the cavity thickness cannot have a negative value ($t_c \geq 0$).
- The cavity starts where the subcavitating pressure crosses the vapor pressure threshold ($P_{sub} = P_V$). This corresponds to the Brillouin-Villat criterion or the smooth detachment criterion.

- Subsequently, the transpiration velocity v^* as well as the cavity thickness t_c is calculated by using Equations 2 and 3.
- The cavity is closed when the cavity thickness returns to zero ($t_c = 0$).
- After the cavity closure point, the transpiration velocity is set to zero ($v^* = 0$) once again. Of course, this is due to the fact that the cavity thickness cannot be negative.

In this way, the cavity length only depends on the pressure distribution in subcavitating conditions and on the vapor pressure. Neither an additional cavity closure model nor empirical parameters are required.

The adaptive factor k which intervenes in the model (Equation 2 or 4) is determined iteratively. Having observed the linear effect of the factor k on the resulting pressure distribution, the iterative procedure used is based on the secant method. The criterion is to obtain the vapor pressure at the maximum cavitation thickness location. Examples of the resulting pressure distribution during an iterative procedure are shown in Figure 2.

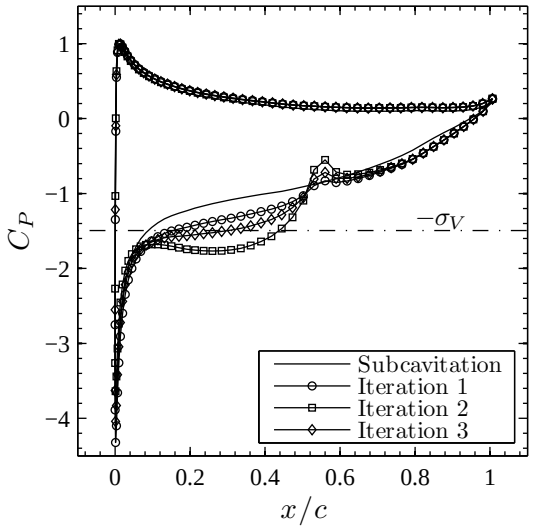

Figure 2: Pressure distribution variation due to different values of the adaptive factor k on a 2D hydrofoil during an iterative procedure

In this paper, the cavitation model has been implemented within two different potential flow codes: a 2D steady-state potential flow with boundary layer simulation and a 3D unsteady-state potential flow.

2.1 Implementation within a 2D steady potential flow code with boundary layer effect

The 2D potential flow code with boundary layer simulation was developed in the study presented in Leroux (2003) and Leroux et al. (2003). This 2D potential flow code takes into account the confinement effect by using the images theory. Furthermore, it uses the transpiration velocities to simulate the boundary layer which is computed using an integral boundary layer representation

code. As already presented above, these transpiration velocities are also used to represent the sheet cavitation. Nevertheless, it remains to be decided how the boundary layer on the sheet cavitation should be modeled. Literature review on the subject shows some disagreement among experimental observations (Dupont and Avellan, 1991; Brewer and Kinnas, 1997); instead of adding a level of complexity with a sub-model, it is decided to inhibit the boundary layer model where the sheet cavitation is present. The boundary layer is modeled normally from the stagnation point to the trailing edge on the pressure side. On the cavitating suction side, the computation procedure is presented as follows:

- The transpiration velocities representing the laminar boundary layer are present from the stagnation point to the sheet cavitation inception point.
- From the cavity detachment point to its closure point, the transpiration velocities representing the boundary layer are set to zero. Hence, the boundary layer is considered to have a constant thickness.
- Once the sheet cavitation has closed itself, the boundary layer computation is resumed in the turbulent mode with its present thickness.

This "boundary layer – sheet cavitation" coupling diagram is presented in Figure 3. The method could be improved but it is always preferable to choose the simplest solution. Furthermore, the current procedure allows to model both the boundary layer and the sheet cavitation in the same simulation.

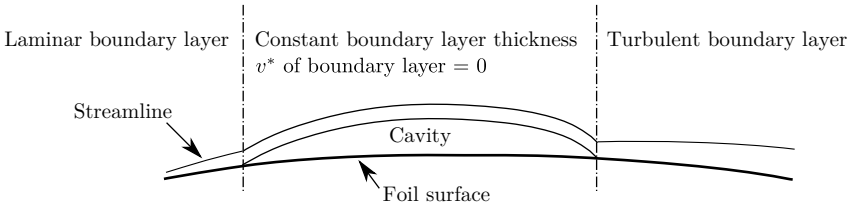

Figure 3: The coupling method between the sheet cavitation model and boundary layer model

The cavitation model is implemented in this 2D potential flow code in order to validate the cavitation model with the experimental data of the 2D cavitating hydrofoil tests from Leroux (2003). The comparison results are presented in Section 3.1.

2.2 Implementation within a 3D unsteady potential flow code

The 3D unsteady potential flow code used for all the 3D simulations in this paper is part of what Hoeijmakers refers to as the second generation potential flow codes in his exhaustive presentation of the different existing potential flow codes in Hoeijmakers (1992). The code uses a Dirichlet condition to force the inner body potential function. The inner and outer body flow models are connected at the frontier, the body surface. The wet surfaces are discretized into quadrilateral panels carrying constant distributions of sources and dipoles. The downstream wakes of lifting bodies, propeller blades or foils are modeled by a sheet of quadrilateral panels carrying constant dipoles distributions. The wake is generated in a Lagrangian manner allowing for unsteady simulations.

Since the cavitation model is defined on a streamline, an assumption is needed to implement the model within the 3D potential flow code. It is assumed that the perturbation velocities are small compared to the upstream velocities. This assumption allows the implementation of the cavitation model in each band (section) of the lifting bodies, propeller blades or foils. Furthermore, it is decided that the adaptive factor k has a different value in each band.

The adaptive factor k in each band is determined independently from the factor k in the other bands with a secant method as in the 2D case. This way, the sheet cavitation model is treated somehow like a strip method. However, the determination of the dipole distribution to satisfy the Kutta-Joukowski condition is carried out in a 3D manner. The relaxation method used imposed that the change of the factor k in each band is forced to not exceed 5% of the value in the previous iteration as shown in Equation 5.

$$\begin{aligned} &\text{if} \quad k_{it+1} > 1.05\, k_{it} \quad \text{then} \quad k_{it+1} = 1.05\, k_{it} \\ &\text{if} \quad k_{it+1} < 0.95\, k_{it} \quad \text{then} \quad k_{it+1} = 0.95\, k_{it} \end{aligned} \tag{5}$$

Moreover, for the reason of unsteady-state flow simulations, another assumption is required. Forced by the principle of the model, it is needed to assume that the vapor inertia due to the phase change is negligible compared to the pressure fluctuation in subcavitating conditions. Hence, the cavity can adapt immediately to the surrounding pressure distribution and does not depend on the previous time-step cavity shape.

3 Validation of cavitation model

In this section, the first stage of validation is presented. The cavitation model is validated by comparing its numerical results with the experimental data and other numerical results available in literature. There are two cases presented here: the comparison with measured pressure coefficients on a 2D hydrofoil and the comparison with measured cavity lengths on a 3D hydrofoil.

3.1 Comparison with measured pressure coefficients over a 2D hydrofoil

Experimental trials of a cavitating 2D hydrofoil have been performed in a cavitation tunnel and presented in Leroux (2003) and Leroux et al. (2003). The conditions of the trials are sufficiently documented to be used for a validation of the sheet cavitation model. These trials have already been used for this purpose by several model developers; see for instance Leroux et al. (2005). In this study, the measured pressure coefficients obtained for various cavity lengths are used to validate the present cavitation model.

In summary, the instrumented hydrofoil with pressure taps is a NACA66(mod)–312 a=0.8 (relative maximum thickness 12% and maximum camber 2%) with a chord length of 150 mm. The hydrofoil is installed in the square test section (192mm$\times$192mm) of the IRENav-EA3634 cavitation tunnel. Both the flow velocity and the pressure are controlled in the cavitation tunnel. The angle of attack of the hydrofoil is set to 6° and the Reynolds number Re is about 7.5×10^5. For a quantitative comparison with the experimental results as described in Leroux (2003), the correction procedure for the inlet velocity in the trials has to be rigorously applied to all pressure coefficients and all cavitation numbers. Furthermore, Leroux (2003) also shows that for this study the effects of confinement and boundary layer are not negligible and should therefore be taken into account.

Before validating the numerical results in cavitating conditions, it is appropriate to first verify and validate the numerical results in subcavitating conditions. Figure 4(a) confirms the validation of numerical results in subcavitating conditions with the almost perfect correspondence between the measured pressure coefficients and the computed results.

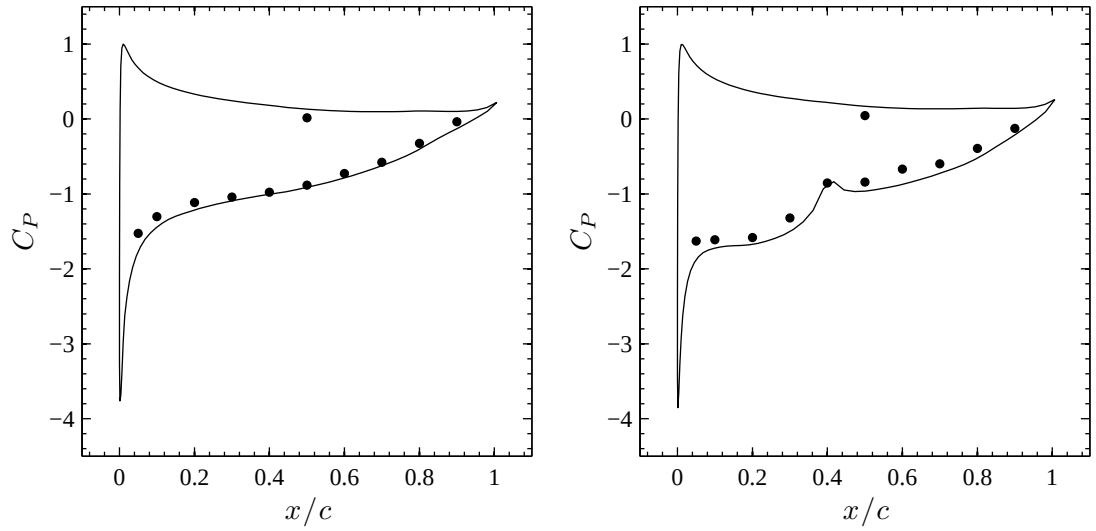

(a) Subcavitating condition

(b) $\sigma_V = 1.622, l_c/C \approx 0.3$

(c) $\sigma_V = 1.541, l_c/C \approx 0.4$

(d) $\sigma_V = 1.495, l_c/C \approx 0.45$

Figure 4: Comparison between the computed (—) and the measured (•) pressure coefficient distribution over the 2D hydrofoil; NACA66(mod)–312 a=0.8 section, $\alpha = 6°$, $Re = 0.75 \times 10^6$

Subsequently, the numerical results in cavitating conditions are compared with the experimental data. For this validation exercise, all the experimental results in cavitating conditions are performed in the same conditions except for the cavitation numbers. The comparison results for the cavitation numbers σ_V of 1.622, 1.541 and 1.495 are presented in Figure 4. The approximate cavity length l_c is 30%, 40% and 45% of the chord length respectively.

With the exception of the first measurement point from the leading edge on the suction side, the numerical results are more than reasonably close to the measurements. In the numerical simulations, a peak of the pressure lower than the vapor pressure near the leading edge is almost always present. In the first analysis, we believe that the peak is mainly due to the Brillouin-Villat cavity detachment criterion, which imposes a continuous tangent between the profile and the sheet cavitation geometry. A refinement of the criterion, either using a critical pressure $P_c < P_V$ with a non-zero cavity detachment curvature slope or by imposing the laminar boundary layer separation as an additional condition, may improve this behavior since the tangent is not observed experimentally. Furthermore, the numerical results of Figure 4(b) (i.e. the smallest cavity length case) are slightly less in agreement with the experimental results than the two others. This may be due to the number of panels inside the cavity.

3.2 Comparison with measured cavity lengths on a 3D hydrofoil

The measurement of cavity lengths on a 3D hydrofoil has been performed at the MIT in their hydrodynamic cavitation tunnel. The 3D elliptical hydrofoil is a windsurf fin designed and built by FINTECH. The details of its geometry and the experimental conditions are presented in Kinnas and Fine (1993).

The exact profile of this FINTECH fin is not specified. Only the spanwise distribution of the leading edge, the trailing edge and the maximum thickness location are given. The position of maximum thickness is around 40% from the leading edge. All the authors who use these experimental results assumed, as it is here, that the section is a NACA65a which is the closest known profile to the FINTECH design.

The trials have been conducted with two different cavitation numbers: σ_V = 1.084 and 1.148. Only the cavity length distribution is measured. Salvatore and Esposito (2001) as well as Peallat and Pellone (1996) also used these experimental results in an attempt to validate their sheet cavitation models. Hence, the present results are not only compared with the experimental data from Kinnas and Fine (1993), but also with the numerical results from Salvatore and Esposito (2001) and Peallat and Pellone (1996).

Unlike the previous 2D case, the confinement and the boundary layer effects are not taken into account. Salvatore and Esposito (2001) as well as Peallat and Pellone (1996) also ignore these effects since only a qualitative comparison is possible – i.e., no forces nor pressure measurements data are available. The comparisons are presented in Figure 5. Despite all the differences of the sheet cavitation models, the detachment criterion and the additional closure submodels, all numerical results are reasonably close to the experimental data.

4 Experimental trials and the final stage validation

In this section, the final stage of the cavitation model validation is presented. Experimental trials in cooperation with the Bulgarian Ship Hydrodynamic Centre (BSHC) were performed. A 3D hydrofoil with a NACA0010 section was installed in the BSHC cavitation tunnel with a force transducer system. The hydrofoil was attached to the upper tunnel wall. A strut with the same section was installed between the hydrofoil and the tunnel wall in order to take the hydrofoil out of the tunnel wall boundary layer. The angle of attack of the strut is always set to zero. Only the forces over the hydrofoil were measured. The dimensions of the hydrofoil, the strut and the tunnel section are presented in Figure 6. The Reynold numbers Re for all the experimental trials are about

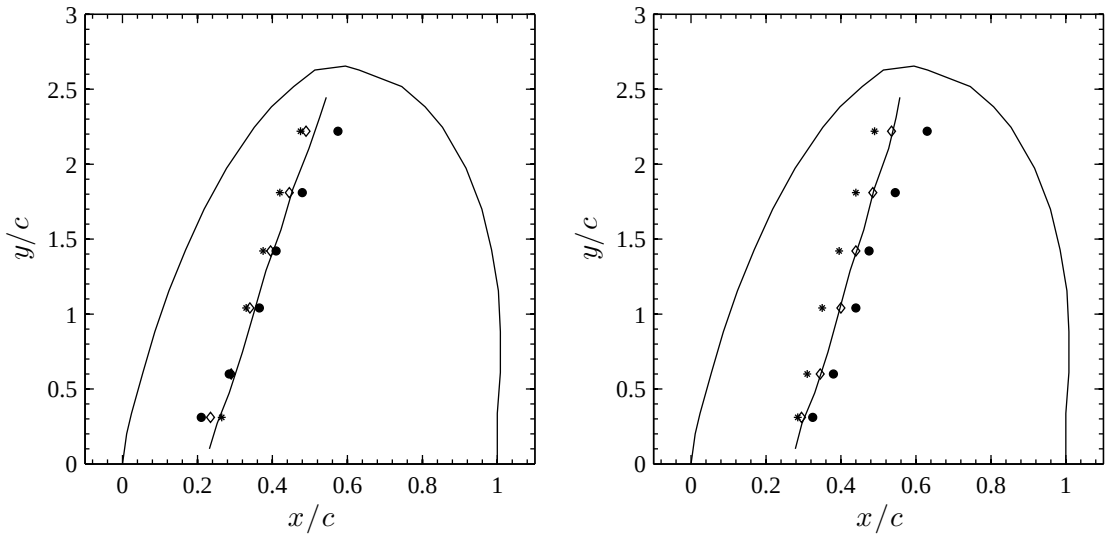

(a) $\sigma_V = 1.148$ (b) $\sigma_V = 1.084$

Figure 5: Comparison between the experimental data and the numerical data of several models of the cavity length distribution on the 3D elliptical fin with NACA65a sections, $\alpha = 6.5°$, the flow comes from the left; (•) experiment, (◇) Salvatore and Esposito (2001), (∗) Peallat and Pellone (1996), (—) present model

1.2×10^6. The experiments were performed in cavitating conditions for five cavitation numbers which correspond approximately to the maximum cavity length of 10%, 20%,30%,40% and 50% of the chord length. The maximum cavity lengths have been estimated visually. The experiments were also performed in subcavitating conditions for three different cavitation numbers. No cavity was observed visually in the subcavitating conditions.

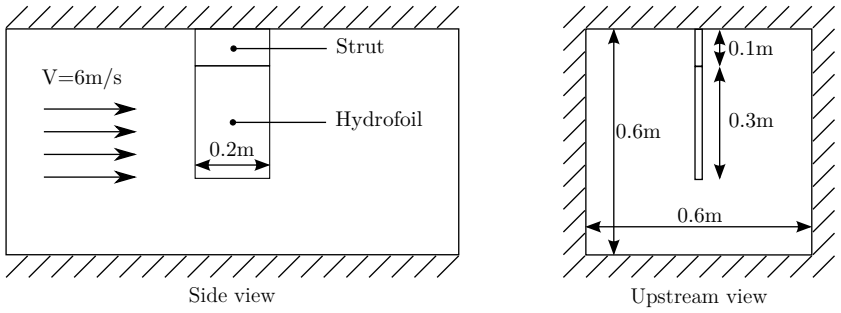

Figure 6: Configuration of the trials performed in the BSHC cavitation tunnel

In the numerical simulations, the upper-tunnel-wall effect is taken into account by using the image theory and the other tunnel walls are represented by flat plates carrying dipoles distribution. The numerical model (meshes of the hydrofoil, the strut and the tunnel wall) is presented in Figure 7. No boundary layer effects are taken into account.

The angle of attack of the hydrofoil is set to 7 degrees ($\alpha = 7°$). However, in order to verify the angle setting system, the measurement of the lift coefficient at the -7 degrees angle of attack in

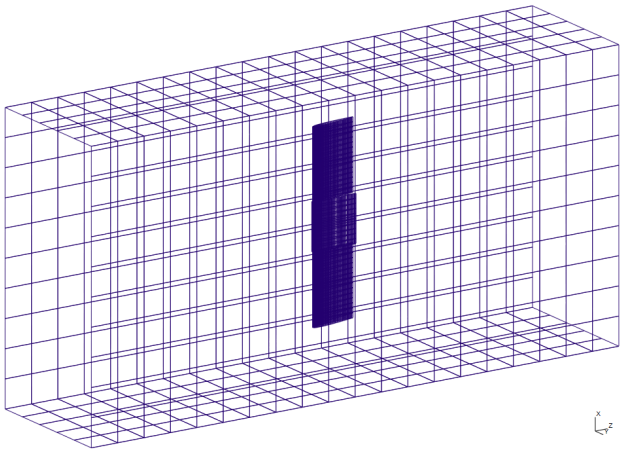

Figure 7: Meshes (without wake panels) used in the numerical simulation

subcavitating conditions is performed as well. The difference of measured lift coefficients between the 7 and -7 degrees of the angle of attack in subcavitating conditions indicates the possibility of a 0.22 degree error in the angle setting. The angle of attack in the numerical simulation is then corrected to 7.22 degrees in order to better approach the experimental setup.

The drag coefficients computed by the potential flow simulation are undoubtedly a lot lower than the measured drag coefficients since only the potential pressure distribution is taken into account. The formula ITTC1957 is then used to estimate the friction forces. All the computed drag coefficients presented in this section are corrected with this ITTC1957 formula.

The comparison results are shown in Figure 8. The error bars are calculated by using the ITTC Recommended Procedures for Uncertainty Analysis in EFD: “7.5-02-01-01 Rev 00 Uncertainty Assessment Methodology” and “7.5-02-01-02 Rev 01 Guidelines for Towing Tank Tests”. The experimental results where the cavitation numbers are higher than 2.5 are considered as in the subcavitating conditions. It is rather a surprise that all the numerical results are smaller than the measured data both in cavitating and subcavitating conditions. Nevertheless, the differences in lift and drag coefficient comparison are less than the uncertainty values.

Figure 9 illustrates the comparison results more visibly in the cavitating zone. The numerical results show the same tendency as the experimental results. The experimental results as well as the numerical results confirm that in the case of partial sheet cavitation, the lift and drag coefficients increase when the cavitation number decreases. Although a small increase in lift coefficient is obtained with the presence of the partial sheet cavitation, the loss is more significant in the lift-to-drag ratio ε_F.

In addition, the numerical drag coefficient graph shows a slope discontinuity around the cavitation number of 1.1. This is most likely due to the numerical high pressure peak at the cavity closure location that reaches the point where the foil surface is tangent with the inlet velocity. In experimental results, the high pressure peak is not observed because the pressure jump is absorbed by cloud cavitation.

Furthermore, photos showing the 3D flow effect over the cavity length distribution have been taken as well. Figure 10 shows the good comparison of the cavity shape between the simulations and the experiments.

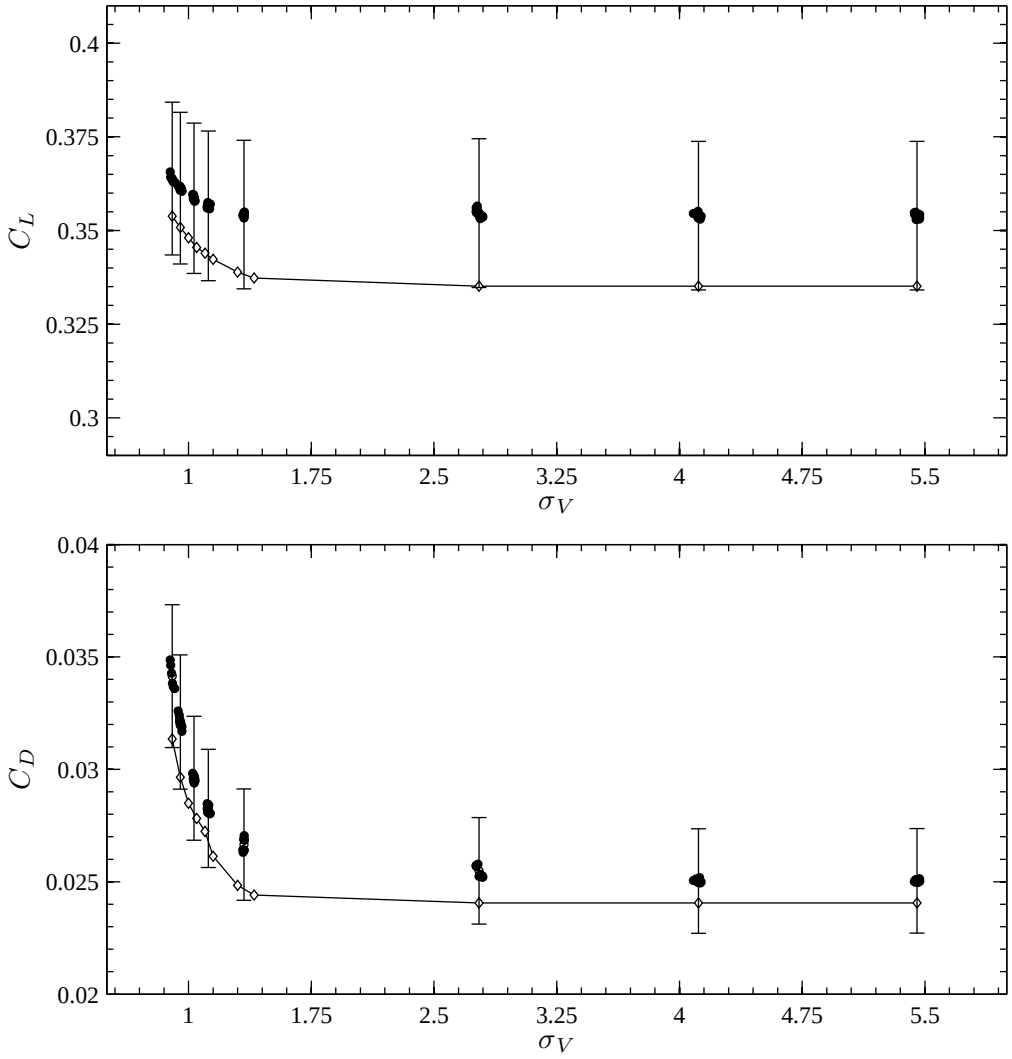

Figure 8: Comparison between the numerical results (–◇–) and the experimental data (•) over the 3D Hydrofoil; NACA0010 section, $\alpha = 7.22°$, $Re \approx 1.2 \times 10^6$

5 Numerical studies

In the previous section, the cavitation model has been well validated using experimental data from hydrofoil tests in steady-state flow conditions. However, in unsteady-state flow conditions as well as for propeller case, with the lack of the experimental data, only the numerical study has been conducted. We first study hydrofoil applications and then continue with propeller applications.

5.1 Hydrofoil working in an oscillating cavitation-number field

In this first numerical study, there is no variation of the pressure distribution in subcavitating conditions. Only the cavitation number is varied. This case is indeed a simplified case of propellers working in the hydrostatic pressure field presented in Section 5.3. The cavita-

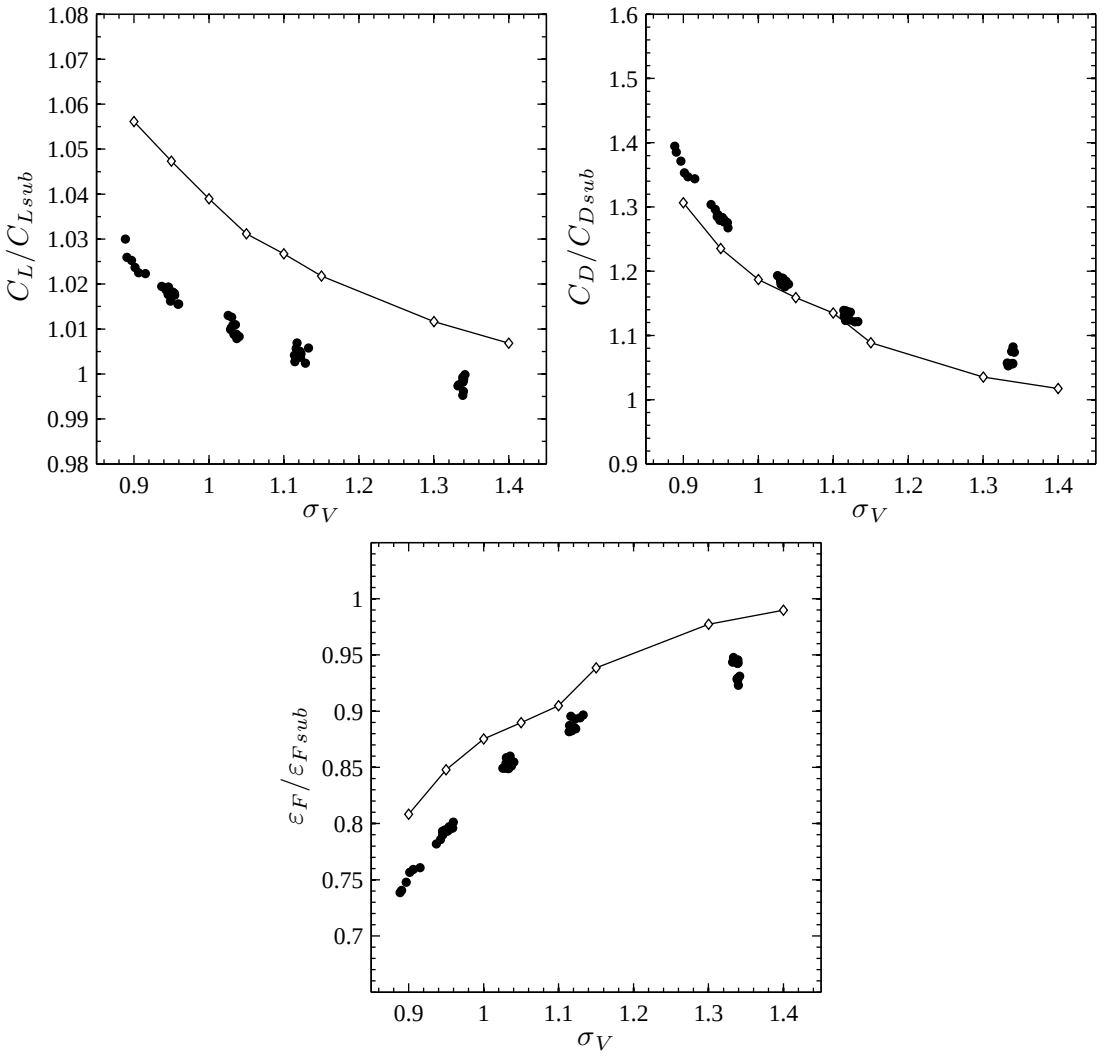

Figure 9: Comparison between the numerical results (–◇–) and the experimental data (•) over the 3D hydrofoil; NACA0010 section, $\alpha = 7.22°$, $Re \approx 1.2 \times 10^6$; the subscript sub refers to subcavitating conditions

tion number σ_V is forced to vary between 0.6823 and 1.1695 in a sinusoidal manner; $\sigma_V = 0.9259 + 0.2436 \sin(\omega t + \phi)$. The given oscillating frequency corresponds to a Strouhal number St of 0.25. The hydrofoil has a NACA0010 section and a rectangular form with an aspect ratio Λ of 3. The angle of attack α is 5 degrees. The numerical model of the hydrofoil has 80 panels along its cross section and 10 panels spanwise.

The results of this simulation are shown in Figure 11. The results in unsteady-state flow conditions are compared with two other results in steady-state flow conditions: with constant cavitation number $\sigma_V = 0.6823$ and in subcavitating conditions. It should be noted that, in both cavitation cases: steady- and unsteady-state flow conditions, the cavitation module is switched on after the convergence of the steady-state subcavitating results. As expected, the lift and drag coefficients vary according to the cavitation number. As already remarked in the validation exercises, the par-

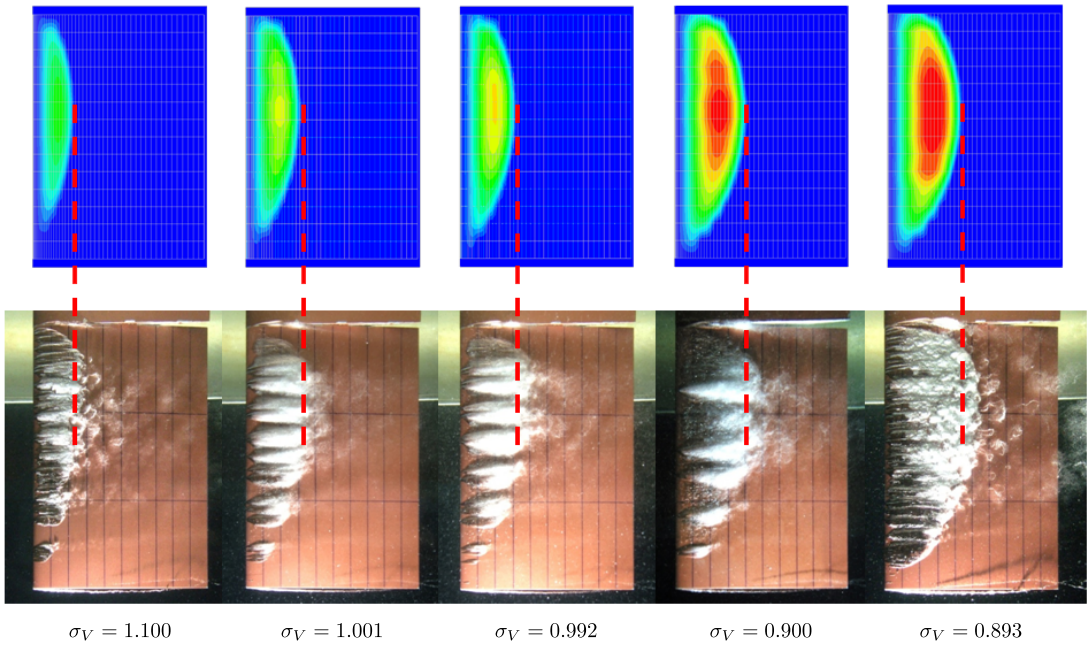

Figure 10: Comparison between the numerical results and the experimental results of cavity shape

tial sheet cavitation has a lot more effect on the drag coefficient than on the lift coefficient. In this case, the lift coefficient changes only by about 6% while the drag coefficient changes by about 50%.

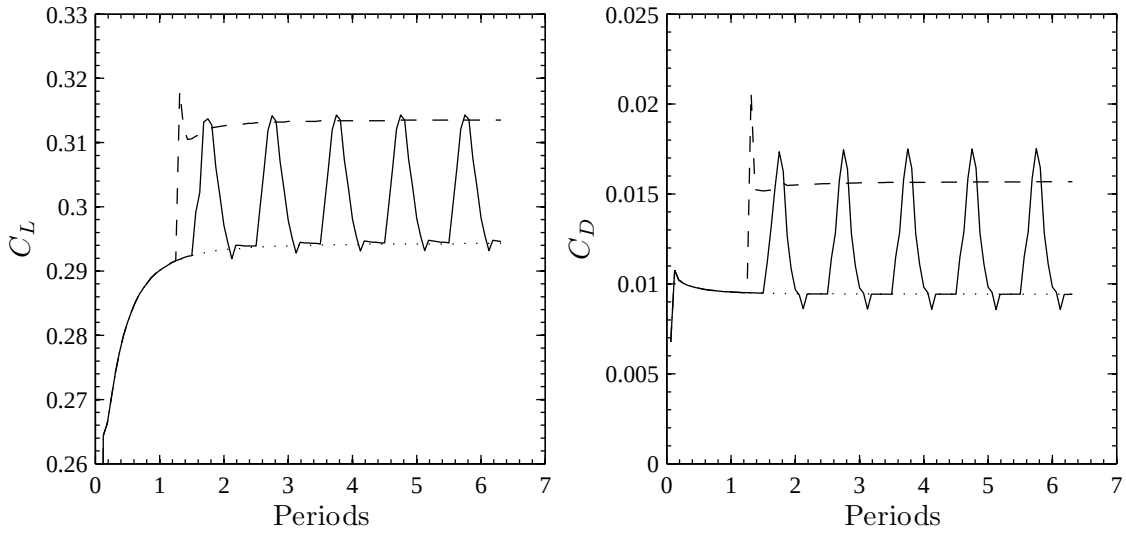

Figure 11: Effect of partial sheet cavitation on lift coefficients C_L and drag coefficients C_D in unsteady-state flow conditions; rectangular hydrofoil, NACA0010 section, $\Lambda = 3$, $\alpha = 5°$, $St = 0.25$; (—) oscillating cavitation number $\sigma_V = 0.9259 + 0.2436 \sin(\omega t)$, (- - -) constant cavitation number $\sigma_V = 0.682$, $(\cdots)$ subcavitating condition

5.2 Hydrofoil with sway motion

Here, we study the case where the pressure distribution in subcavitating conditions varies while the cavitation number ramains constant. This case can be considered as a simplified case of propellers working in an inclined uniform flow presented in Section 5.4. A hydrofoil is forced to move laterally in a uniform flow, as described in Figure 12(a). The sway motion creates the variation of angle of attack as well as the variation of inflow velocity magnitude. The sinusoidal lateral velocity is given in such a way that the angle of attack varies between -5 degrees and 5 degrees as shown in Figure 12(b). The hydrofoil section is also a NACA0010 with 80 panels along its cross section and 10 panels spanwise as in the previous case. However, the aspect ratio Λ in this case is 6 instead of 3 in order to reduce the 3D flow effect for a better capture of the cavitation effect. The cavitation number is constant and equal to 0.65. The Strouhal number St is also 0.25 as in the previous case.

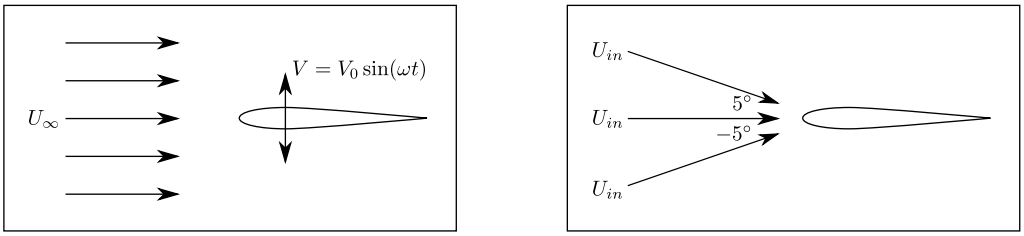

(a) General configuration

(b) Variation of inflow velocity with respect to hydrofoil reference frame

Figure 12: Definition of sway motion problem

Figure 13 shows the lift and drag coefficients of the hydrofoil versus the angle of attack. In quasi-static conditions, the lift coefficient changes linearly with the angle of attack. Notwithstanding, in sway motion, the lift coefficient in subcavitating conditions presents an elliptic curve due to fluid inertia. For the drag coefficient, we obtain the classical parabolic curve in quasi-static conditions. In sway motion, the fluid inertia transforms the parabolic curve into a butterfly shape curve. We can see that the partial sheet cavitation has not much of effect on the lift coefficient curve. However, the effect of cavitation is noticeable on the drag coefficient curve. The cavitation results presented in Figure 13 also demonstrate that the cavitation model can be applied for unsteady-state flow condition cases.

5.3 Propeller working in hydrostatic pressure field

Before studying the effect of sheet cavitation on propeller performance in unsteady-state flow conditions, it is appropriate to study the effect of sheet cavitation in steady-state flow conditions first. A cavitating marine propeller is simulated with several cavitation numbers. It should be note that the cavitation numbers used here for propeller simulations both in steady-state flow conditions and in unsteady-state flow conditions are defined with respect to the upstream velocity or the advanced velocity V_a of the propeller, $\sigma_V = (P_{ref} - P_V)/(\frac{1}{2}\rho V_a^2)$.

The effect of the partial sheet cavitation on thrust coefficient K_T and torque coefficient K_Q as well as on propeller efficiency η in steady-state flow conditions is shown in Figure 14. Like in the hydrofoil cases, with the presence of partial sheet cavitation, the thrust and torque coefficient

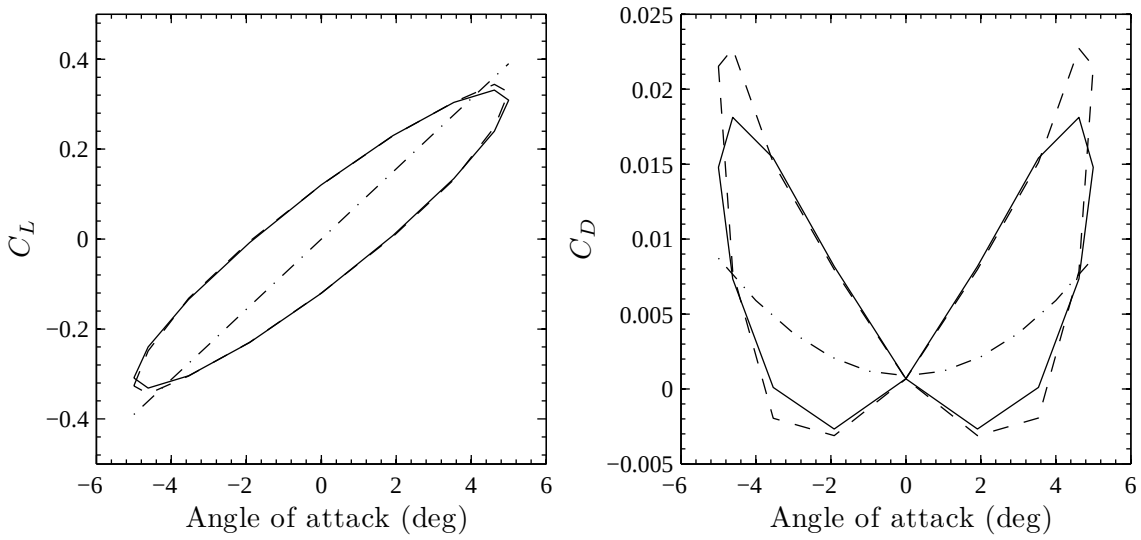

Figure 13: Lift (C_L) and drag (C_D) coefficient in sway motion; rectangular hydrofoil: NACA0010 cross section, Λ = 3, St = 0.25, σ_V = 0.65; (—) subcavitating condition, (- -) cavitating condition $\sigma_V = 0.65$, (- · -) quasi-static subcavitating condition

increase when the cavitation number decreases. However, small effects on thrust coefficients K_T and torque coefficients K_Q are observed. In this particular case, the thrust and torque increase only a few percent even when the cavity length reaches 3/4 of chord length in some sections near the blade tip as shown in Figure 15. Furthermore, the propeller efficiency η hardly decreases. These small effects are expected since the propeller hydrodynamic forces are originated from the section lift and the load distribution is not concentrated in the blade tip zone.

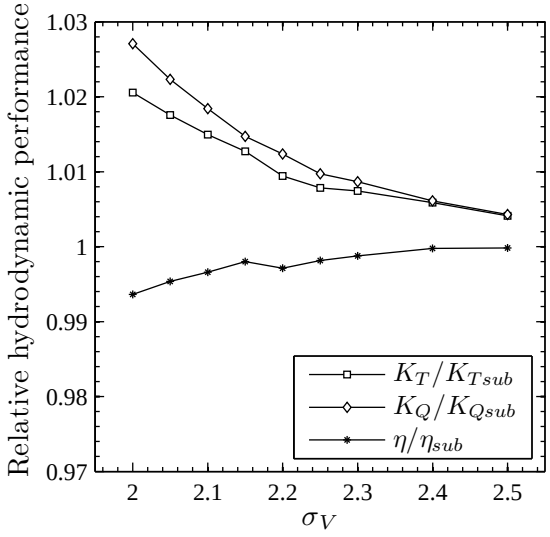

Figure 14: Effect of partial sheet cavitation on thrust coefficient K_T, torque coefficient K_Q and efficiency η of a marine propeller; the subscript sub refers to the results in subcavitating conditions

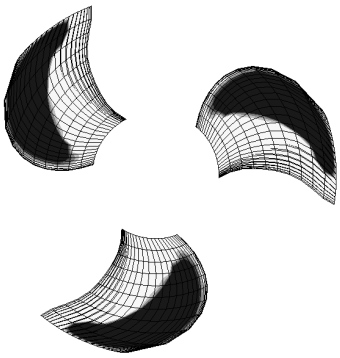

Figure 15: Cavity shape of a marine propeller in steady-state flow conditions, $\sigma_V = 2.0$; the cavity appears in black on the blade

Now the effect of the partial sheet cavitation on propeller performance in unsteady-state flow conditions is studied. The cavitating propeller is at present simulated within a hydrostatic pressure field. The hydrostatic pressure makes the cavitation number to vary with the depth. The configuration is set to have the variation of cavitation number as shown in Figure 16(a). A snapshot of the obtained cavitating propeller is presented in Figure 16(b). The cavity appears and increases in volume when the propeller blades approach to the free surface. Also as expected, the cavity decreases in volume and disappears when the propeller blades move away from the free surface. The appearance and disappearance of the cavity makes the blade thrust and the blade torque coefficient to vary. The variation of thrust and torque coefficient of each propeller blade is presented in Figure 17. There is some numerical noise in the numerical results. The assumption that the cavity does not depend on the previous time-step cavity shape might not be really appropriate and cause some numerical noise. However, the time-average results look reasonable. An example of pressure coefficient distribution on the section $r/R = 0.7$ (R = propeller radius) when the blade is in the upper position (Figure 16(b)) is presented in Figure 18.

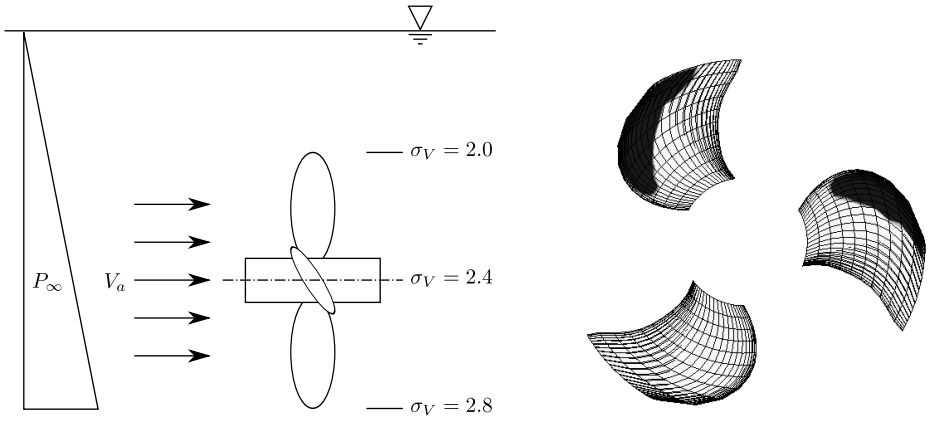

(a) General configuration (b) Cavity shape

Figure 16: Simulation of the cavitating propeller working in a hydrostatic pressure field

Like in the steady-state flow case, the partial sheet cavitation has small effects on hydrody-

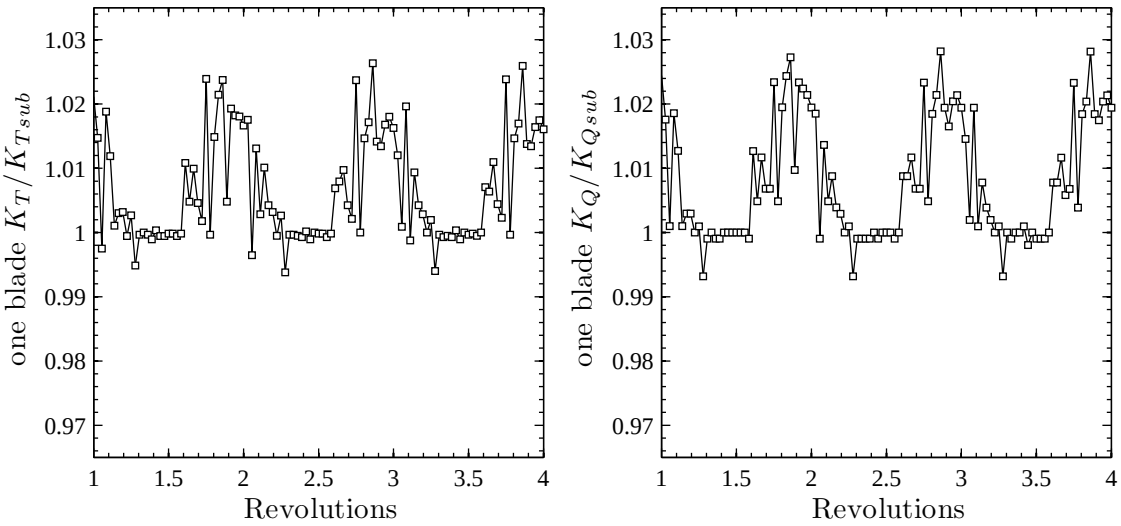

Figure 17: Variation of blade thrust and torque coefficient of the cavitating propeller working in a hydrostatic pressure field; the subscript sub refers to subcavitating conditions

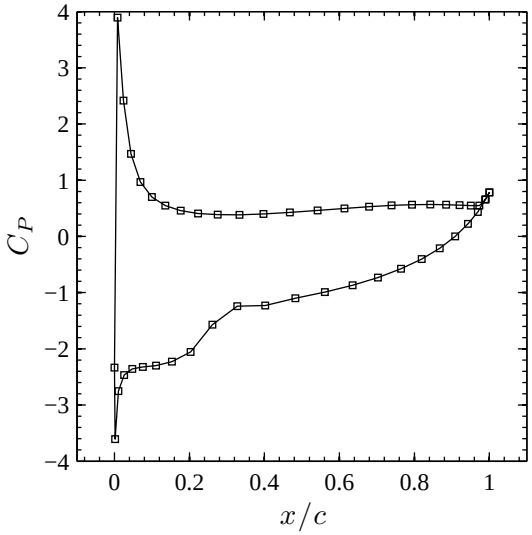

Figure 18: Pressure coefficient distribution on the section $r/R = 0.7$ of the upper blade of the cavitating propeller working in a hydrostatic pressure field

namic forces. Nevertheless, this variation of hydrodynamic forces may combine with other unsteady hydrodynamic forces and may cause the ship vibration as well as the fatigue on propeller shaft and propeller blades.

5.4 Propeller working in an inclined uniform flow

The last simulation presented here is a marine propeller operating in an inclined uniform flow as shown in Figure 19(a). The angle between the upstream uniform flow and the propeller shaft is 5

degrees. As shown in Figure 19(b), the cavity takes place on the starboard side of the propeller. This corresponds to the angle of attack and the inflow velocity magnitude at each section of the propeller blades. It confirms the expectations since both the velocity magnitude and the angle of attack is higher on the starboard side. As previously, small effects are obtained on thrust and torque. Figure 20 shows the variation of thrust coefficient during a revolution both in subcavitating conditions and cavitating conditions. It is obvious that the cavitation occurs when propeller blade is very loaded. The effect of the partial sheet cavitation in this particular case strengthens the subcavitating unsteady hydrodynamic forces.

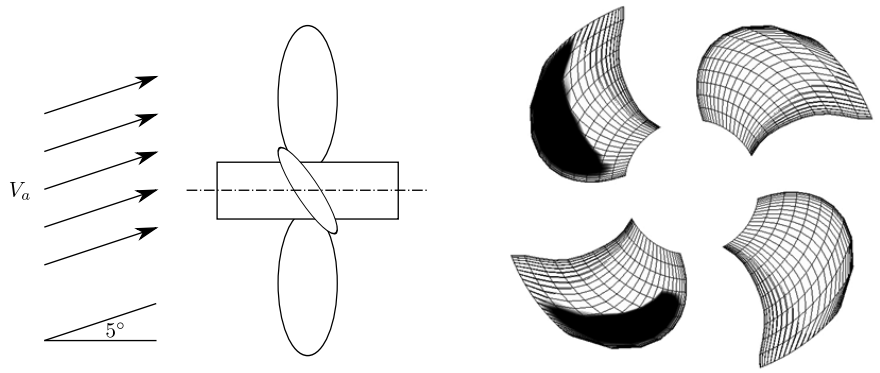

(a) General configuration (b) Cavity shape

Figure 19: Simulation of the cavitating propeller working in an inclined uniform flow

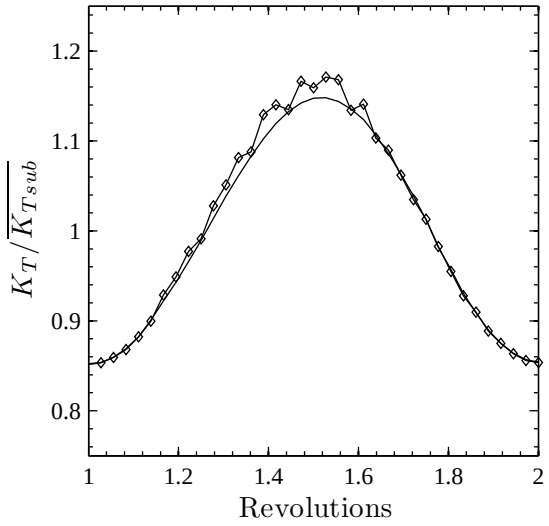

Figure 20: One-blade thrust coefficient of the cavitating propeller working in an inclined uniform flow; (—) in subcavitating conditions, (–◇–) in cavitating conditions; $\overline{K_{Tsub}}$ refers to the average of the one-blade thrust coefficient in subcavitating conditions